Solid State Communications 152 (2012) 1301–1305

Contents lists available at SciVerse ScienceDirect

Solid State Communications

journal homepage: www.elsevier.com/locate/ssc

Quantum transport in double-gated graphene devices

J. Velasco Jr., Y. Lee, L. Jing, G. Liu, W. Bao, C.N. Lau *

Department of Physics and Astronomy, University of California, Riverside, CA 92521, USA

ARTICLE INFO

Article history:
Accepted 12 April 2012
by L. Brey
Available online 25 April 2012

Keywords:
A. Graphene
B. Dual gates
C. pn Junctions
D. Quantum Hall effect

ABSTRACT

Double-gated graphene devices provide an important platform for understanding electrical and optical properties of graphene. Here we present transport measurements of single layer, bilayer and trilayer graphene devices with suspended top gates. In zero magnetic fields, we observe formation of pnp junctions with tunable polarity and charge densities, as well as a tunable band gap in bilayer graphene and a tunable band overlap in trilayer graphene. In high magnetic fields, the devices' conductance are quantized at integer and fractional values of conductance quantum, and the data are in good agreement with a model based on edge state equilibration at pn interfaces.

© 2012 Elsevier Ltd. All rights reserved.

1. Introduction

As an electron system, graphene [1–3] has many unique properties not found in conventional semiconductor heterostructures [4–7]. For instance, the honeycomb lattice has two atoms per unit cell, giving rise to a new quantum number, pseudospin, and chiral charge carriers. Another important consequence of the honeycomb lattice is the unusual band structure: single layer graphene has a linear energy dispersion relation, thus the charge carriers behave as chiral massless particles; these particles are akin to neutrinos (but with charge e) or photons (but with spin ½). Moreover, due to graphene's atomic thickness, separation between adjacent sub-bands is much larger than conventional two-dimensional electron systems (2DES); thus phenomena that traditionally only emerge at dilution refrigerator temperatures become readily accessible at much higher temperatures, enabling studies that would be otherwise difficult or impossible.

An important characteristic of graphene is that, because of its zero band gap, its charge density and type are tunable via electrostatic means. A unique device configuration enabled by graphene is a double-gated geometry, consisting of graphene positioned between a global back gate (typically provided by the doped Si substrates) and a metallic top gate. By modulating voltages applied to both gates, one can create regions with different dopant levels and types in a single graphene device, thus realizing pnp junctions with tunable junction polarity. For bilayer and trilayer graphene, the presence of two gates also enable independent tuning of total charge density and out-of-plane electric field that breaks the inversion symmetry of few-layer graphene [8–20]. In the past few years, double-gated graphene devices have become a fascinating platform that harbors a plethora of novel phenomena, such as Klein tunneling [21–25], Fabry–Pérot oscillations [24,26], edge state equilibration [27–30] and localization-induced conductance fluctuations [31] in the quantum Hall regime, band gap opening in bilayer [13,14,16,18–20], stacking-dependent band gap or band overlap in trilayer graphene [32–34] and observation of states with spontaneous broken symmetries in bilayer graphene [35–37].

Here we describe and discuss our transport measurements on single layer (SLG), bilayer (BLG) and trilayer (TLG) graphene devices with double-gated geometry. The article is organized as follows. Section 2 describes fabrication of devices with suspended top gates using a multi-level lithography technique, where the absence of dielectric material (other than vacuum) enables synthesis of high mobility devices. Sections 3– 5 present and discuss transport measurements in SLG, BLG and TLG devices, respectively, in both zero and finite magnetic fields. Lastly, we conclude with a brief summary and outlook in Section 6.

2. Fabrication

Since graphene consists of only a single atomic layer of carbon, deposition of top gate materials may introduce defects, dopants or additional scattering sites, which obscure many of the most fascinating physical phenomena. Previously, materials such as electron beam resists [29] or alternating layers of NO_2, trimethylaluminum and Al_2O_3 [25,27] have been used as the dielectrics for local gates. We developed a multi-level lithography technique to fabricate 'air-bridge'-styled top gates, in which a metallic bridge is suspended across a portion of the graphene sheet, with vacuum acting as the dielectric. A similar technique was also reported by

* Corresponding author.
E-mail address: lau@physics.ucr.edu (C.N. Lau).

0038-1098/$ - see front matter © 2012 Elsevier Ltd. All rights reserved.
http://dx.doi.org/10.1016/j.ssc.2012.04.024

Ref. [38]. Because graphene is only exposed to conventional lithographical resists and developers during fabrication, this technique minimizes the damage to the atomic layer. Most importantly, the absence of a top gate dielectric allows post-fabrication annealing [39] to further improve device quality.

The substrate consists of a 300 nm SiO_2 layer grown over degenerately doped silicon that functions as a global back gate. Graphene sheets are then deposited onto the substrate by the standard micro mechanical exfoliation method, and the layer number is identified by the color contrast in an optical microscope and verified by Raman spectroscopy [40].

To fabricate the air bridge, we employ a resist bilayer with different exposure and developing conditions, so as to create a temporary support for the suspended structure; this resist support is subsequently removed after triple-angle metal depositions at -45, 45 and 0°. The details of the fabrication procedure are discussed in [26,30]. Finally, using standard electron beam lithography, electrodes are deposited consisting of 10 nm of Ti and 80 nm of Al or Au on graphene. To ensure a robust suspension of the air bridge with none to minimal sagging, a critical point dryer is typically used during fabrication of the top gate and electrodes. As shown by the scanning electron microscope (SEM) image of a finished device in Fig. 1(a), the top gate is suspended above the graphene sheet between source and drain electrodes. We note that it is important to fabricate the electrodes in the last step, since contact resistance tends to deteriorate during lithographical processes.

Since no dielectric material directly contacts the single atomic layer, these graphene devices are exceedingly clean. The air-gap between the top gate and graphene also allows surface absorbates, including those directly under the top gate, to be removed via annealing [26,30]. A demonstration of this is shown in Fig. 1(b), where we measure the two-terminal conductance G of a graphene device as a function of applied back gate voltage V_{bg} both before and after annealing in vacuum at 120 °C. Clearly the $G(V_{bg})$ characteristics are considerably improved upon annealing, with a sharper Dirac point that is closer to zero, indicating the removal of undesirable absorbates and resist residue.

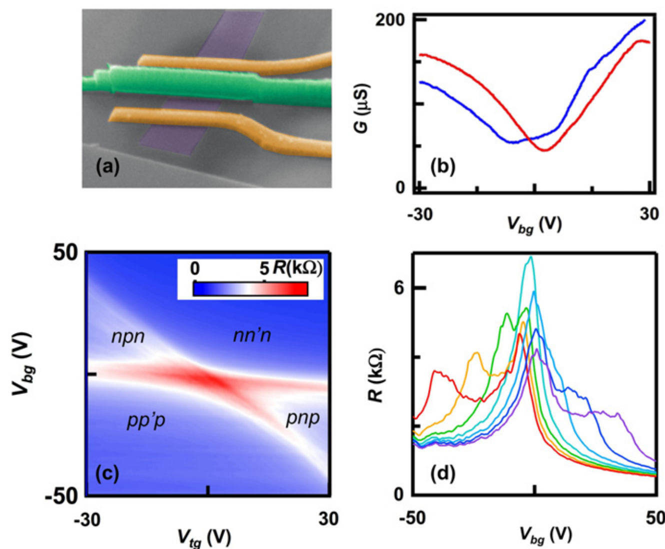

Fig. 1. (Color online) Device image and data of SLG at $B=0$. (a). SEM image of a graphene device with a suspended top gate. (b). $G(V_{bg})$ of a typical graphene graphene before (blue line) and after (red line) annealing. (c). $R(V_{bg},V_{tg})$ of a double-gated SLG device. (d). Line traces through (c) at, from purple to red, $V_{tg}=-30$, -20, -10, 0, 10, 20, 29.5 V, respectively.

3. Single layer graphene pnp junctions

By modulating voltages applied to back gate V_{bg} and top gate V_{tg}, a graphene pnp junction can be created. In a typical device, the source drain electrode separation is $L\sim1$–4 μm, and the width of the graphene sheet is $W\sim0.4$–1.5 μm; the contactless top gate straddles the center portion of the sheet with a width of $\sim$0.5 μm, and is suspended at a distance d$\sim$50–200 nm above the substrate. Since it only covers the center portion of the graphene sheet, the top gate is local. Charge densities in the uncovered regions, or region 1, are only controlled by voltages applied to the back gate V_{bg},

$$n_1 = C_{bg}(V_{bg}-V_{bg}^D)/e, \tag{1a}$$

whereas those in the top-gated region (or region 2) are modulated by both gates,

$$n_2 = n_1 + C_{tg}(V_{tg}-V_{tg}^D)/e. \tag{1b}$$

Here C_{bg} (C_{tg}) is the capacitance per unit area between graphene and the back gate (top gate), V_{bg}^D and V_{tg}^D are the charge neutrality points (CNP) in the "bare" and top-gated regions, respectively, and e the electron charge. For a typical device on Si/SiO_2 substrates, the gate coupling factor $\alpha_{bg}=n_1/V_{bg}\sim7.2\times10^{10}$ cm^{-2}. All devices are measured in a He^3 refrigerator at base temperature $T=260$ mK using standard lock-in techniques. The electrical lines in the refrigerator are outfitted with 3 stages of filters to ensure low noise and low electron temperature.

To investigate the device behavior in zero magnetic field, we measure its two-terminal resistance R as a function of V_{bg} at different values V_{tg}. The representative curves are shown in Fig. 1(c) from a device with mobility $\sim$10,000 cm^2/V s. At $n_1=n_2=0$, the device is at its global charge neutrality point, reaching a global resistance maximum $R_{max}\sim7$ kΩ. With increasing $|V_{tg}|$, R_{max} decreases to $\sim$4 kΩ, and a prominent side peak develops; the portion of the $R(V_{bg})$ curves between the 2 peaks corresponds to the behavior of a bipolar (pnp *or* npn) junction. These features can be more easily seen in the two-dimensional plot in Fig. 1(d), which plots R(color) as functions of V_{bg} (vertical axis) and V_{tg}(horizontal axis). The horizontal and diagonal red lines indicate local resistance maxima and correspond to the CNP of region 1 and region 2, respectively. The slope of the diagonal line yields the ratio C_{tg}/C_{bg}, and is often used to determine the top gate's coupling factor α_{tg}. Taken together, these 2 lines partition the plot into four regions with different dopant combinations–pnp, pp′p, npn and nn′n, thus demonstrating a graphene pnp junction with tunable junction polarity.

In high magnetic fields the cyclotron orbits of charge carriers in graphene coalesce to form Landau levels (LLs) with energies [4,5,7]

$$E_{SLG} = \pm\sqrt{2\hbar v_F^2 eB|N|} \tag{2}$$

Between the LLs, the two-teminal device conductance is quantized at

$$G = 4\left(N+\frac{1}{2}\right)\frac{e^2}{h} \equiv \upsilon\frac{e^2}{h} \tag{3}$$

where h is Planck's constant, v_F is the Fermi velocity, $N=\ldots-1$, 0, 1,… is an integer indicating the LL index, and $\nu=nh/Be$ is the filling factor. The factor of 4 denotes a degeneracy from spin and sublattice degrees of freedom. A signature of graphene's relativistic energy dispersion is the presence of a LL at $E_N=0$, which is equally occupied by electrons and holes resulting in quantum Hall plateau that are quantized at half of integer N values of $4e^2/h$.

This energy spectrum of graphene is reflected in transport measurements in finite B. A typical data set is shown in Fig. 2(a),

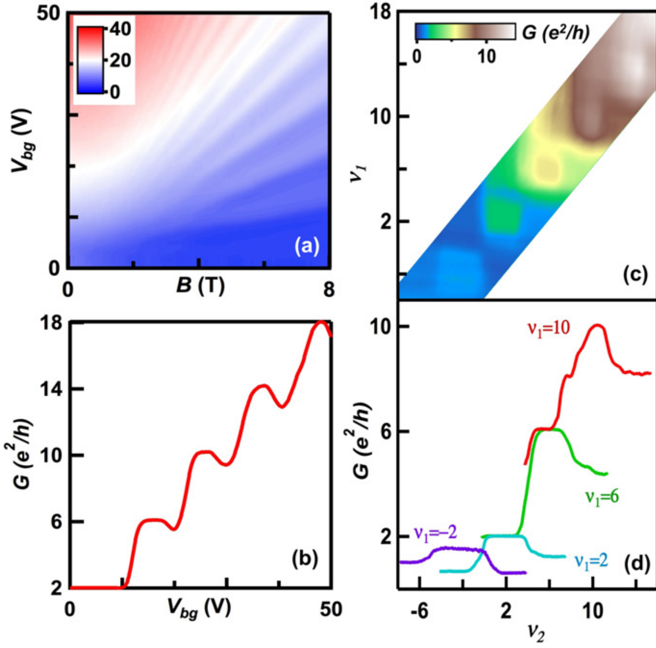

Fig. 2. (Color online) Data from a SLG pnp junction in the quantum Hall regime. (a). $G(V_{bg}, B)$ of a SLG device. (b). $G(V_{bg})$ of the device at $B=8$ T. (c). $G(\nu_1, \nu_2)$ of a SLG at $B=8$ T. (d). Line traces $G(\nu_2)$ at $\nu_1=-2$, 2, 6 and 10.

which plots G as a function of V_{bg} and B (the top gate is disconnected). The quantum Hall states appear as the LL fan that radiate from $B=0$ and the CNP. At $B=8$ T, the device conductance $G(V_{bg})$ is quantized at 2, 6, 10, 14 and 18 e^2/h (Fig. 2(b)), suggesting relatively small broadening of LL up to $N=4$ and indicating the high quality of the sample. We also note that the slope of the plateaus in the V_{bg}-B plane is given by $\nu e/\alpha_{bg}h$, and can be used to extract α_{bg}.

A local dual gated device allows regions with different doping and polarities. As a result, its quantum Hall conductance is not necessarily quantized at integer values of e^2/h, due to the presence of counter-propagating edge states. Instead, G depends on the relative values of n_1 and n_2, and can have fractional values of e^2/h. A simple model was proposed by Ref. [29], assuming perfect edge state equilibration at the interfaces between different regions: for a unipolar junction ($n_1 n_2 > 0$) with $|\nu_1| \geq |\nu_2|$, the non-top-gated regions act as reflection-less contacts to the center region, yielding a device conductance

$$G = e^2/h|\nu_1|, \quad (4)$$

where ν_1 and ν_2 are the filling factors in the region 1 and 2, respectively. If instead $|\nu_2| > |\nu_1|$, the conductance is,

$$G = e^2/h(1/|\nu_1| - 1/|\nu_2| + 1/|\nu_1|)^{-1} \quad (5)$$

For a bipolar junction ($n_1 n_2 < 0$), the device behaves simply as three resistors in series,

$$G = e^2/h(1/|\nu_1| + 1/|\nu_2| + 1/|\nu_1|)^{-1} \quad (6)$$

The two-terminal G data of a local dual gated graphene device $B=8$ T is shown in Fig. 2(c) as functions of ν_1 (vertical axis) and ν_2 (horizontal axis). The most striking feature of the plot is the series of rectangles with different colors, representing quantum Hall plateaus at different combinations of ν_1 and ν_2. The robust appearance of the various conductance plateau up to an orbital level of $N=2$ underscores the high quality of this sample. Line traces $G(\nu_2)$ at $\nu_1=-2$, 2, 6 and 10 are displayed in Fig. 2(d), with conductance values in excellent agreement with those calculated by Eqs. (4)–(6). For instance, for $\nu_1=2$, $G=0.67$ at $\nu_2=-2$, $G=2$ at $\nu_2=2$, and $G=1.2$ at $\nu_2=6$. Thus our data demonstrate partial and full equilibration of co- and counter-propagating edge states.

4. Bilayer graphene pnp junctions

The band structure of a pristine bilayer graphene is parabolic, $E=(\hbar^2 k^2)/2m^*$, where $m^*=0.02$–$0.04\ m_e$ and m_e is the electron's rest mass, with the conduction and valence bands touching at the inequivalent K and K' points[8–11]. Similar to SLG, applying V_{bg} and V_{tg} creates a pnp junction in bilayer graphene with modulation of junction polarity and dopant level. A typical data set is shown in Fig. 3(a), displaying two-terminal R (color in a logarithmic scale) as functions of V_{bg} (vertical axis) and V_{tg}(horizontal axis) for a device with electron mobility $\sim$10,000 cm^2/V s. In this device, the top gate straddles the center portion of the flake at a distance $d\sim 50$ nm above with a width of 0.5 μm.

It is instructive to compare this data set with the SLG data in Fig. 1(c). Both plots are partitioned into 4 quadrants of different junction polarities, with the diagonal line that indicate the resistance maximum $R_{\max}$ at the CNP of region 2. The striking difference between the plots is the change in *magnitude* of $R_{\max}$ — in SLG $R_{\max}$ varies by only $\sim$50%, while in BLG, $R_{\max}$ changes by more than a factor of 100, reaching as high as 1 MΩ (Fig. 3(b)).

This unusual behavior of the BLG pnp junction arises from opening of a band gap in the BLG energy spectrum[8,11–20]. What distinguishes dual-gated BLG from their SLG counterparts is that application of voltages to the two gates not only controls densities n_1 and n_2, but also an electric field E_2 applied across the bilayer in the top-gated region. This electric field is given by

$$E_2 = [\varepsilon_{\rm sio}(V_{bg} - V_{bg}^D)/t - (V_{tg} - V_{tg}^D)/d]/2 \quad (7)$$

where $\varepsilon_{\rm sio}\sim$ 3.9 and $t=300$ nm are the dielectric constant and thickness of the SiO_2 layer, respectively. Such an out-of-plane electric field breaks BLG's inversion symmetry and creates a potential difference between the two layers, $V_2=E_2(3.3$ Å). As a result, the band structure of BLG adopts the Mexican hat profile, with an induced gap $\Delta=(t_\perp eV_2)/(\sqrt{t_\perp^2+e^2V_2^2})$ that scales

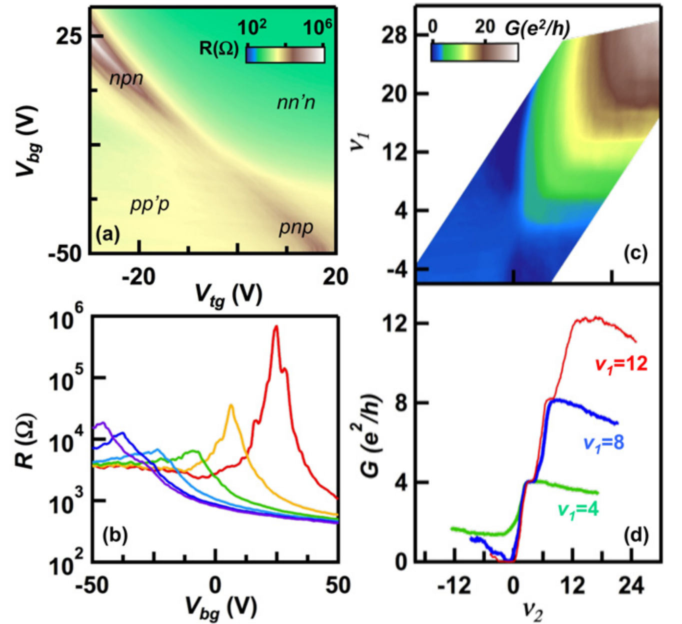

Fig. 3. (Color online) Transport data from a BLG pnp junction. (a). $R(V_{bg}, V_{tg})$ of the BLG device at $B=0$. Note that the logarithmic color scale. (b). Line traces through (a) at, from red to purple, $V_{tg}=-30$, -20, -10, 0, 10 and 15 V, respectively. (c). $G(\nu_1, \nu_2)$ of the device at $B=8$ T. (d). Line traces $G(\nu_2)$ at $\nu_1=4$, 8 and 12.

linearly with V_2 for small V_2, and saturates at $t_\perp$ when V_2 is sufficiently large. Here $t_\perp \sim 0.2$–0.4 eV is the inter-layer hopping energy.

The highly resistive state observed in the upper left corner of Fig. 3(a) thus arises from the gap opening at large E_2. On the other hand, though E_2 as high as 1 V/nm is applied, the device never becomes truly insulating (e.g., resistance does not exceed 1 MΩ), as one would expect from the opening of a gap as large as 0.2 eV. This discrepancy is due to the presence of localized states that either lie within the gap [41–44] or are formed from disorder-induced charge puddles [45,46], and transport across the junction has been shown to be variable range hopping at low temperatures and thermal activation at high temperature [14,17,18,20].

In high magnetic fields, LLs in BLG have energies

$$E^{BL} = \pm \frac{\hbar eB}{m^*}\sqrt{N(N-1)} \quad (8)$$

Between the LLs, the device conductance is quantized at

$$G = 4N(e^2/h) \quad (9)$$

where the LL index $N = \ldots -3, -2, -1, 1, 2, 3\ldots$. Notably, the $N=0$ and $N=1$ Landau levels are degenerate, resulting in the 8-fold degeneracy at $E=0$.

The quantum Hall conductance of a BLG pnp junction at $B=8$ T is shown in Fig. 3(c). Just as the case for SLG, the presence of regions with different densities gives rise to co- or counter-propagating edge states, which equilibrate at the junction interfaces. This results in regions with different conductance values, appearing as bands of colors in Fig. 3(c). The conductance values are also given by Eqs. (4)–(7), with one important difference – instead of $-6, -2, 2, 6\ldots$, the filling factors ν_1 and ν_2 are $-8, -4, 4, 8\ldots$etc. As shown in Fig. 3(d), line traces $G(\nu_2)$ at $\nu_1 = 4$, 8, and 12 are in reasonable agreement with theoretical calculations [20].

Finally, we note that in the absence of broken degeneracy, the smallest quantum Hall conductance of BLG is $4e^2/h$ for a uniform junction, and $4/3e^2/h$ for a pnp junction. In contrast, an insulating state appears in Fig. 3(c), as represented by the dark blue region. This insulating state emerges at high B and E_2, and is an indication of the competing symmetries in BLG. It is also intimately related to the intrinsic insulating state in ultra-clean BLG [36,37], the nature of which has been a topic of intense debate to date [47–56].

5. Trilayer graphene pnp junctions

Trilayer graphene has two stable configurations, ABA and ABC stackings, which differ only in the relative positions of the top-most and bottom layers. As the name suggests, in ABA-stacked TLG the top and bottom layers are AA-stacked, whereas in ABC-stacked they are Bernal-stacked. These 2 allotropes have dramatically different band structures [32,57–62] and electrical and optical properties [32–34,63–66], and can be experimentally identified via infrared or Raman spectroscopy [63,67].

Here we will focus on only ABA-stacked TLG, which is estimated to consist of ~85% of all graphene devices. Its band structure is expected to be a combination of SLG's linear dispersion and BLG's quadratic dispersion. Like BLG, it is susceptible to effects of an out-of-plane electric field E_2; but instead of the tunable band *gap* in BLG, ABA-stacked TLG is predicted to have a tunable band overlap [32,57–62]. Such effects can be seen from transport data of double-gated TLG devices that are verified to be ABA-stacked via Raman spectroscopy (Fig. 4(a). Fig. 4(b) displays the resistance R (color) through a TLG pnp device with suspended top gates as functions of V_{bg} (vertical axis) and V_{tg} (horizontal axis). The global Dirac point of the device is found to be at $V_{bg} = -7.8$ and $V_{tg} = 13.5$ V. Fig.4(c) displays the line traces $R(V_{bg})$ at different V_{tg} values. For V_{tg} at the Dirac point, the $R(V_{bg})$ curve has the characteristic inverse V-shape, with an estimated mobility 4000 cm^2/V s. As V_{tg} shifts away from the Dirac point, i.e., with increasing E_2, the maximum resistance $R_{\max}$ decreases, indicating an increasing band overlap, in agreement with previously reported work[32].

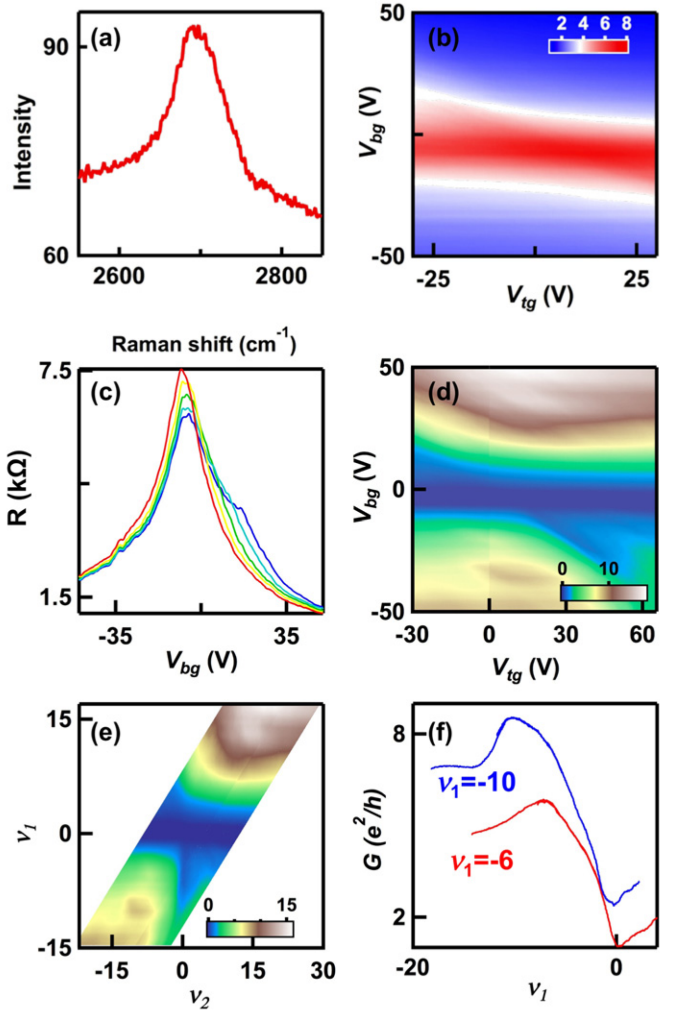

Fig. 4. (Color online) Raman and transport data from a TLG pnp junction. (a). Raman spectrum of the TLG device. (b). $R(V_{bg}, V_{tg})$ in kΩ of the TLG device at $B=0$. (c). Line traces through (b) at, from red to blue, $V_{tg} = 13.5$ (CNP), 0, 10, 20, and 28 V, respectively. (d). $G(V_{bg}, V_{tg})$ in units of e^2/h of the TLG device at $B=8$ T. (e). Data in (d) replotted as functions of ν_1 and ν_2. (d). Line traces $G(\nu_2)$ at $\nu_1 = -6$ (red) and -10 (blue).

In magnetic fields, from tight-binding calculations that keep only the nearest-layer coupling term, the Landau level spectrum for ABA-stacked trilayer [9,57,68,69] is a superposition of those for SLG and BLG, i.e., a combination of Eqs. (2) and (8).

The LL at zero energy is 12-fold degenerate, giving rise to quantized conductance plateaus with integer values$\ldots -10$, -6, 6, 10, 14$\ldots$ of e^2/h. When other interlayer coupling terms are included (γ_2–γ_5 in the Slonczewski–Weiss–McClure parametrization of graphite), some of the degeneracies are expected to be broken. However, the LL at zero energy is expected to retain at least 2-fold degeneracy.

Fig. 4(d) displays G (in units of e^2/h) of the TLG device at $B=8$ T as functions of V_{bg} (vertical axis) and V_{tg} (horizontal axis). Notably, an insulating state $\nu=0$ was observed, indicating partial lifting of the 12-fold degeneracy. We note that this is the first

time that the insulating state is observed in ABA-stacked TLG, and realization of a pnp junction in a trilayer device. To compare with SLG and BLG devices in the quantum Hall regime, we replot the data in Fig. 4(d) as functions of ν_1 and ν_2 (Fig. 4(e)), which resembles Figs. 2(c) and 3(c). Line traces $G(\nu_2)$ at $\nu_1=-6$ and -10 are shown in Fig. 4(f). We find that the conductance values are only in semi-quantitative agreement with Eqs. (4)–(6). For instance, for $\nu_1=-10$, G is expected to reach $10e^2/h$ at $\nu_2=-10$ and decreasing to $\sim 7.8e^2/h$ at $\nu_2=-14$ and $\sim 6.9e^2/h$ at $\nu_2=-18$. From the blue trace in Fig. 1(f), $G\sim 8.5e^2/h$ at $\nu_2=-10$, and $\sim 6.9e^2/h$ at $\nu_2=-18$, but with no discernible plateau at $\nu_2=-14$. Such discrepancy between the model and data is likely due to the relatively low mobility of the TLG device, and is expected to be diminished or eliminated with improved device quality.

6. Conclusion

Graphene and its few layer cousins constitute a unique electron system, and double-gated graphene devices have been a particularly attractive platform for investigation of electrical properties in zero magnetic field and in the quantum Hall regime. An important frontier in this area is ultra-clean double-gated graphene devices, which can be fabricated by suspending graphene or use of boron nitride as the top and bottom gate dielectrics [70,71]. Many novel phenomena, both predicted and unforeseen, are expected to emerge in these ultra-clean systems. Examples include possible phase transitions driven by electric and magnetic fields in BLG and TLG, interactions among edge states with broken degeneracies and in ballistic devices, and Klein tunneling in few layer graphene. Thus, we expect double-gated graphene devices will continue to offer much insight into low dimensional quantum systems.

Acknowledgement

The authors acknowledge the support by NSF CAREER DMR/0748910, NSF DMR/1106358, NSF ECCS/0926056, ONR N00014-09-1-0724, ONR/DMEA H94003-10-2-1003 and the FENA Focus Center. CNL acknowledges the support by the “Physics of Graphene” program at KITP.

References

[1] K.S. Novoselov, A.K. Geim, S.V. Morozov, D. Jiang, Y. Zhang, S.V. Dubonos, I.V. Grigorieva, A.A. Firsov, Science 306 (2004) 666.
[2] K.S. Novoselov, A.K. Geim, S.V. Morozov, D. Jiang, M.I. Katsnelson, I.V. Grigorieva, S.V. Dubonos, A.A. Firsov, Nature 438 (2005) 197.
[3] Y.B. Zhang, Y.W. Tan, H.L. Stormer, P. Kim, Nature 438 (2005) 201.
[4] A.K. Geim, K.S. Novoselov, Nat. Mater. 6 (2007) 183.
[5] A.H. Castro Neto, F. Guinea, N.M.R. Peres, K.S. Novoselov, A.K. Geim, Rev. Mod. Phys. 81 (2009) 109.
[6] M.S. Fuhrer, C.N. Lau, A.H. MacDonald, MRS Bull. 35 (2010) 289.
[7] S. Das Sarma, S. Adam, E.H. Hwang, E. Rossi, Rev. Mod. Phys. 83 (2011) 407.
[8] E. McCann, Phys. Rev. B 74 (2006) 161403.
[9] E. McCann, V.I. Fal'ko, Phys. Rev. Lett. 96 (2006) 086805.
[10] K.S. Novoselov, E. McCann, S.V. Morozov, V.I. Fal'ko, M.I. Katsnelson, U. Zeitler, D. Jiang, F. Schedin, A.K. Geim, Nat. Phys. 2 (2006) 177.
[11] E.V. Castro, K.S. Novoselov, S.V. Morozov, N.M.R. Peres, J. Dos Santos, J. Nilsson, F. Guinea, A.K. Geim, A.H. Castro Neto, Phys. Rev. Lett. 99 (2007) 216802.
[12] A.B. Kuzmenko, I. Crassee, D. van der Marel, P. Blake, K.S. Novoselov, Phys. Rev. B 165406 (2009).
[13] J.B. Oostinga, H.B. Heersche, X.L. Liu, A.F. Morpurgo, L.M.K. Vandersypen, Nat. Mater. 7 (2008) 151.
[14] F.N. Xia, D.B. Farmer, Y.M. Lin, P. Avouris, Nano Lett. 10 (2010) 715.
[15] K.F. Mak, C.H. Lui, J. Shan, T.F. Heinz, Phys. Rev. Lett. 102 (2009) 256405.
[16] Y.B. Zhang, T.T. Tang, C. Girit, Z. Hao, M.C. Martin, A. Zettl, M.F. Crommie, Y.R. Shen, F. Wang, Nature 459 (2009) 820.
[17] T. Taychatanapat, P. Jarillo-Herrero, Phys. Rev. Lett. 105 (2010) 166601.
[18] J. Yan, M.S. Fuhrer, Nano Lett. 10 (2010) 4521.
[19] K. Zou, J. Zhu, Phys. Rev. B 081407 (2010).
[20] L. Jing, J. Velasco Jr., P. Kratz, G. Liu, W. Bao, M. Bockrath, C.N. Lau, Nano Lett. 10 (2010) 4000.
[21] V.V. Cheianov, V.I. Fal'ko, Phys. Rev. B 74 (2006) 041403.
[22] M.I. Katsnelson, K.S. Novoselov, A.K. Geim, Nat. Phys. 2 (2006) 620.
[23] A.V. Shytov, M.S. Rudner, L.S. Levitov, Phys. Rev. Lett. 101 (2008) 156804.
[24] A.F. Young, P. Kim, Nat. Phys. 5 (2009) 222.
[25] N. Stander, B. Huard, D. Goldhaber-Gordon, Phys. Rev. Lett. 102 (2009) 026807.
[26] J. Velasco, G. Liu, W.Z. Bao, C.N. Lau, New J. Phys. 11 (2009) 095008.
[27] J.R. Williams, L. DiCarlo, C.M. Marcus, Science 317 (2007) 638.
[28] D.A. Abanin, L.S. Levitov, Science 317 (2007) 641.
[29] B. Ozyilmaz, P. Jarillo-Herrero, D. Efetov, D.A. Abanin, L.S. Levitov, P. Kim, Phys. Rev. Lett. 99 (2007) 166804.
[30] G. Liu, J. Velasco, W.Z. Bao, C.N. Lau, Appl. Phys. Lett. 92 (2008) 203103.
[31] J. Velasco, G. Liu, L. Jing, P. Kratz, H. Zhang, W.Z. Bao, M. Bockrath, C.N. Lau, Phys. Rev. B 81 (2010) R121407.
[32] M.F. Craciun, S. Russo, M. Yamamoto, J.B. Oostinga, A.F. Morpurgo, S. Thrucha, Nat. Nanotechnol. 4 (2009) 383.
[33] C.H. Lui, Z. Li, K.F. Mak, E. Cappelluti, T.F. Heinz, Nat. Phys. 7 (2011) 944.
[34] E.A. Henriksen, D. Nandi, J.P. Eisenstein, Phys. Rev. X 2 (2012) 011004.
[35] R.T. Weitz, M.T. Allen, B.E. Feldman, J. Martin, A. Yacoby, Science 330 (2010) 812.
[36] W. Bao, J.V. Jr., F. Zhang, L. Jing, B. Standley, D. Smirnov, M. Bockrath, A. MacDonald, C.N. Lau, preprint, 〈arXiv:1202.3212v1〉 (2012).
[37] J. Velasco, L. Jing, W. Bao, Y. Lee, P. Kratz, V. Aji, M. Bockrath, C.N. Lau, C. Varma, R. Stillwell, D. Smirnov, F. Zhang, J. Jung, A.H. MacDonald, Nat. Nanotechnol. 7 (2012) 156.
[38] R.V. Gorbachev, A.S. Mayorov, A.K. Savchenko, D.W. Horsell, F. Guinea, Nano Lett. 8 (2008) 1995.
[39] J. Moser, A. Barreiro, A. Bachtold, Appl. Phys. Lett. 91 (2007) 163513.
[40] A.C. Ferrari, J.C. Meyer, V. Scardaci, C. Casiraghi, M. Lazzeri, F. Mauri, S. Piscanec, D. Jiang, K.S. Novoselov, S. Roth, A.K. Geim, Phys. Rev. Lett. 97 (2006) 187401.
[41] T.O. Wehling, A.V. Balatsky, A.M. Tsvelik, M.I. Katnelson, A.I. Lichtenstein, Europhys. Lett. 84 (2008) 17003.
[42] M.I. Katsnelson, M.F. Prokhorova, Phys. Rev. B 77 (2008) 205424.
[43] F. Guinea, M.I. Katsnelson, M.A.H. Vozmediano, Phys. Rev. B 77 (2008) 075422.
[44] J. Nilsson, A.H. Castro, Phys. Rev. Lett. 98 (2007) 126801.
[45] J. Martin, N. Akerman, G. Ulbricht, T. Lohmann, J.H. Smet, K. v. Klitzing, A. Yacoby, Nat. Phys. 4 (2008) 144.
[46] A. Deshpande, W. Bao, F. Miao, C.N. Lau, B.J. LeRoy, Phys. Rev. B 79 (2009) 205411.
[47] H. Min, G. Borghi, M. Polini, A.H. MacDonald, Phys. Rev. B 77 (2008) 041407.
[48] R. Nandkishore, L. Levitov, Phys. Rev. B 82 (2010) 115124.
[49] F. Zhang, J. Jung, G.A. Fiete, Q.A. Niu, A.H. MacDonald, Phys. Rev. Lett. 106 (2011) 156801.
[50] J. Jung, F. Zhang, A.H. MacDonald, Phys. Rev. B 83 (2011) 115408.
[51] F. Zhang, H. Min, M. Polini, A.H. MacDonald, Phys. Rev. B 81 (2010) 041402(R).
[52] Y. Lemonik, I.L. Aleiner, C. Toke, V.I. Fal'ko, Phys. Rev. B 82 (2010) 201408.
[53] O. Vafek, K. Yang, Phys. Rev. B 81 (2010) 041401.
[54] E.V. Castro, N.M.R. Peres, T. Stauber, N.A.P. Silva, Phys. Rev. Lett. 100 (2008) 186803.
[55] I. Martin, Y.M. Blanter, A.F. Morpurgo, Phys. Rev. Lett. 100 (2008) 036804.
[56] M. Kharitonov, *preprint*, 〈arXiv:1105.5386v1〉 (2011).
[57] F. Guinea, A.H. Castro Neto, N.M.R. Peres, Phys. Rev. B 73 (2006) 245426.
[58] M. Aoki, H. Amawashi, Sol. State Commun. 142 (2007) 123.
[59] F. Zhang, B. Sahu, H.K. Min, A.H. MacDonald, Phys. Rev. B 82 (2010) 035409.
[60] B. Partoens, F.M. Peeters, Phys. Rev. B 74 (2006) 075404.
[61] A.A. Avetisyan, B. Partoens, F.M. Peeters, Phys. Rev. B 80 (2009) 195401.
[62] A.A. Avetisyan, B. Partoens, F.M. Peeters, Phys. Rev. B 81 (2010) 115432.
[63] K.F. Mak, J. Shan, T.F. Heinz, Phys. Rev. Lett. 104 (2010) 176404.
[64] W. Bao, L. Jing, Y. Lee, J.V. Jr., P. Kratz, D. Tran, B. Standley, M. Aykol, S.B. Cronin, D. Smirnov, M. Koshino, E. McCann, M. Bockrath, C.N. Lau, Nat. Phys. 7 (2011) 948.
[65] L. Zhang, Y. Zhang, J. Camacho, M. Khodas, I. Zaliznyak, Nat. Phys. 7 (2011) 953.
[66] T. Taychatanapat, K. Watanabe, T. Taniguchi, P. Jarillo-Herrero, Nat. Phys. 7 (2011) 621.
[67] C.H. Lui, Z. Li, Z. Chen, P.V. Klimov, L.E. Brus, T.F. Heinz, Nano Lett. 11 (2011) 164.
[68] J.W. McClure, Phys. Rev. 104 (1956) 666.
[69] M. Ezawa, J. Phys. Soc. Jpn. 76 (2007) 094701.
[70] C.R. Dean, A.F. Young, I. Meric, C. Lee, L. Wang, S. Sorgenfrei, K. Watanabe, T. Taniguchi, P. Kim, K.L. Shepard, J. Hone, Nat. Nano 5 (2010) 722.
[71] L.A. Ponomarenko, A.K. Geim, A.A. Zhukov, R. Jalil, S.V. Morozov, K.S. Novoselov, I.V. Grigorieva, E.H. Hill, V.V. Cheianov, V.I. Fal'ko, K. Watanabe, T. Taniguchi, R.V. Gorbachev, Nat. Phys. 7 (2011) 958.